

# Distribution of Cracks in an Anchored Cavern Under Blast Load Based on Cohesive Elements

Yi Luo

Wuhan University of Technology

Chenhao Pei

Wuhan University of Technology

Dengxing Qu (✉ [dengxingqu@whut.edu.cn](mailto:dengxingqu@whut.edu.cn))

Wuhan University of Technology

Xinping Li

Wuhan University of Technology

Ruiqiu Ma

Wuhan University of Technology

Hangli Gong

Wuhan University of Technology

---

## Research Article

**Keywords:** blast load, anchored caverns, crack propagation, cohesive elements with zero thickness, numerical simulation

**Posted Date:** December 6th, 2021

**DOI:** <https://doi.org/10.21203/rs.3.rs-1100159/v1>

**License:**  This work is licensed under a Creative Commons Attribution 4.0 International License.

[Read Full License](#)

---

**Version of Record:** A version of this preprint was published at Scientific Reports on March 16th, 2022. See the published version at <https://doi.org/10.1038/s41598-022-08560-y>.

---

## Distribution of cracks in an anchored cavern under blast load based on cohesive elements

Yi Luo<sup>a,b,d</sup>, Chenhao Pei<sup>a,b</sup>, Dengxing Qu<sup>c\*</sup>, Xinping Li<sup>a,b,d</sup>, Ruiqiu Ma<sup>a,b</sup>, Hangli Gong<sup>a,b</sup>

(<sup>a</sup> School of Civil Engineering and Architecture, Wuhan University of Technology, Wuhan, 430070, China; <sup>b</sup> Hubei Key Laboratory of Road-bridge and Structure Engineering, Wuhan University of Technology, Wuhan, 430070, China; <sup>c</sup> School of Safety Science and Emergency Management, Wuhan University of Technology, Wuhan, 430070, China; <sup>d</sup> Sanya Science and Education Innovation Park of Wuhan University of Technology, Sanya, 572000, China)

**Abstract:** To explore the distribution of cracks in anchored caverns under the blast load, cohesive elements with zero thickness were employed to simulate crack propagation through numerical analysis based on a similar model test. Furthermore, the crack propagation process in anchored caverns under top explosion was analysed and the distribution and mode of propagation of cracks in anchored caverns when a fracture with different dip angles was present in the vault were discussed. With the propagation of the explosive stress waves, cracks successively occur at the boundary of the anchored zone of the vault, arch foot, and floor of the anchored caverns. Tensile cracks are preliminarily found in rocks surrounding the caverns. In the case that a pre-fabricated fracture is present in the upper part of the vault, the number of cracks at the boundary of the anchored zone of the vault decreases, then increases with increasing dip angle of the pre-fabricated fracture. The fewest cracks at the boundary of the anchored zone occur if the dip angle of the pre-fabricated fracture is 45°. The wing cracks deflected to the vault are formed at the tip of the pre-fabricated fracture, around which tensile and shear cracks are synchronously present. Under top explosion, both the peak displacement and peak particle velocity in surrounding rocks of anchored caverns reach their maximum values at the vault, successively followed by the side wall and the floor. In addition, they show asymmetry with the difference of the dip angle of the pre-fabricated fracture; the vault displacement of anchored caverns is mainly attributed to the formation of tensile cracks at the boundary of the anchored zone generated due to tensile waves reflected from the free face of the vault. When a fracture is present in the vault, the peak displacement of the vault decreases while the residual displacement increases.

**Keywords:** blast load, anchored caverns, crack propagation, cohesive elements with zero thickness, numerical

---

27 simulation.

## 28 **1 Introduction**

29       Underground engineering works are affected by dynamic loading, such as the blast load generated during  
30 excavation of adjacent tunnels<sup>[1,2]</sup>, accidental blast load<sup>[3]</sup>, or missile attack<sup>[4]</sup>. In addition, some defects (i.e.  
31 faults and joints) are inevitably present in the rock surrounding an underground caverns, as shown in Fig. 1.  
32 Fractures affect the stability of underground structures under blast load; especially, when open through-going  
33 fractures (such as faults, joints, and excavation-induced cracks) appear, not only do these fractures affect crack  
34 propagation in the vicinity of anchored caverns, but primary fractures may interact and even coalesce with other  
35 cracks in anchored caverns. Thus, it is necessary to explore crack propagation around anchored caverns with  
36 pre-existing fractures under dynamic load.



37

38

Fig. 1 Cave rock mass fracture

39       At present, research into the dynamic response of underground anchored caverns has attracted  
40 much attention. Scholars have investigated the failure modes of underground anchored caverns  
41 without pre-existing fractures. Xu et al.<sup>[5]</sup> and Wang et al.<sup>[6]</sup> investigated the failure of anchored caverns  
42 under blast load through physical model testing. Sivalingam et al.<sup>[7]</sup> surveyed the stress redistribution  
43 around adjacent tunnels during blasting excavation. Xia et al.<sup>[8]</sup> conducted field tests and numerical  
44 simulations. Li et al.<sup>[9]</sup> analysed the influence of waves triggered by blast tunnelling with explosive  
45 charges on the peak particle velocity (PPV) and stress from adjacent tunnels. Scholars also have  
46 explored the damage and failure of underground anchored caverns with pre-existing fractures. Liu et

---

47 al.<sup>[10]</sup> investigated the propagation of fractures around tunnels under blast load through use of a  
48 TMCSC model. Zhou et al.<sup>[11]</sup> explored the propagation characteristics of radial fractures in tunnels  
49 under the effect of impact load. Based on dynamic testing, Guo et al.<sup>[12]</sup> investigated crack propagation  
50 in roadways with defects under blast load. As for failure characteristics of joint planes in rocks under  
51 dynamic load, Yang et al.<sup>[13]</sup> analysed the crack propagation path, the changes in stress intensity factor,  
52 and wing-crack mechanism of different joints. Li <sup>[14]</sup> determined certain characteristics of the  
53 interaction between stress waves and rock joints. With the aid of numerical analysis software,  
54 Deng<sup>[15]</sup> analysed the extent, severity, and modes of failure in a circular roadway with joints under  
55 dynamic blast load.

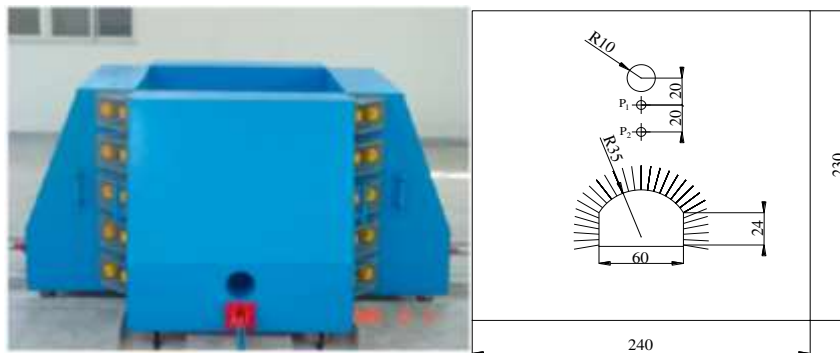
56 Many scholars concentrate on the dynamic propagation of fractures or small-scale approximate  
57 tests<sup>[16,17,18]</sup>. The large-scale physical testing of anchored caverns under blast load is expensive and  
58 requires time. According to physical test data, the distribution and propagation of cracks in anchored  
59 caverns with a pre-existing fracture were explored through use of the numerical simulation methods.  
60 Due to the discontinuity and complexity of fractures, it is difficult to simulate crack propagation using  
61 the finite element method. In current research, cracks are approximately expressed mainly through  
62 element deletion or element damage<sup>[19,20]</sup>. Having low computational efficiency for a large-scale  
63 model, the particle flow code, discrete element and extended finite element methods are applicable  
64 for exploring test blocks at experimental scale<sup>[21,22,23]</sup>. Cohesive element has the advantages of high  
65 computational efficiency and good convergence in analyzing crack propagation<sup>[24,25]</sup>. Based on  
66 cohesion model, many scholars have studied concrete<sup>[26,27,28,29]</sup> and rock<sup>[30,31]</sup> at meso scale, and  
67 analyzed the fracture process of rock like materials. The existing research on the dynamic response of  
68 anchored caverns mainly focuses on stress, displacement and vibration velocity, and there is little  
69 research on the crack propagation of anchored caverns. By globally embedding cohesive elements  
70 with zero thickness, the crack propagation process in surrounding rocks of anchored caverns was  
71 analysed; moreover, the distribution of cracks and modes of failure of anchored caverns when a pre-

72 fabricated fracture with different dip angles was present in the vault were investigated.

## 73 2 Calculation model

### 74 2.1 Establishment of the model

75 To verify the accuracy of the embedded cohesive elements with zero thickness, a calculation  
76 model was established according to the physical test model. The test equipment is shown in Fig. 2 and  
77 details are provided elsewhere [6]. For convenience of calculation, the physical test model was  
78 simplified into a plane strain problem. The calculation model is illustrated in Fig. 3. The model has  
79 dimensions of 2400 mm × 2300 mm × 40 mm (width × height × thickness), in which the cavern,  
80 appearing as a circular arch with vertical walls, presents a span of 60 cm and a height of 40 cm,  
81 showing the radius of the circular arch of 35 cm; the spacing between bolts, each with a length of 24  
82 cm, is set to 4 cm. The centre of the blast source is 83 cm from the top of the cavern. At the left and  
83 right-hand boundaries and the lower part of the model, semi-infinite bodies are simulated with an  
84 infinite element. The bolt elements and surrounding rocks are simultaneously deformed, and the bolts  
85 and the slippage effect thereof are simulated by bilinear constitutive model.



86

87 Fig. 2 The test device

87 Fig. 3 Schematic representation of the calculation model (unit: cm)

88 As we are interested in the crack distribution in the rock surrounding an anchored cavern, The  
89 air action near the explosion area is not considered, the blast pressure was measured by the test and  
90 applied to the blasting cavity at 10 cm from the centre of the explosive charge. The time history curve  
91 of pressure is shown in Fig. 4.

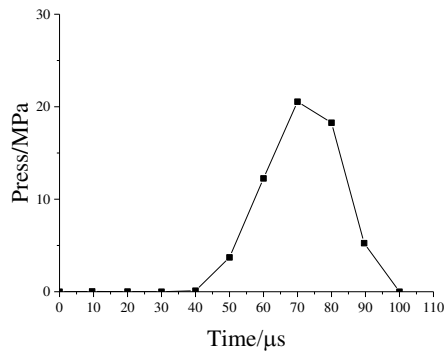


Fig. 4 Explosion pressure time history curve

92

93

## 94 2.2 Constitutive model

95

96

97

98

99

100

101

102

103

104

105

Cohesion essentially refers to the interaction between material atoms or molecules. As a simplified phenomenological model, the cohesive zone model (CZM) visualises the crack initiation and propagation. In terms of its core concept, the non-linear constitutive model of materials is described based on the relationship between cohesion and relative displacement. The bilinear CZM is applied here, for which it is supposed that materials in the cohesive zone are linear-elastic in the initial response stage; thereafter, linear damage begins to evolve in the materials once the initial damage reaches its critical value, that is, the criterion denoting onset of the initial damage. The response of the model materials during failure is mainly reflected by using cohesive elements, therefore, quite a large stiffness is used to allow complete transmission of force from solid elements in the elastic stage. The response of model materials after reaching peak stress is simulated by utilising the descending segment of the stress-strain relationship for these cohesive elements.

106

107

108

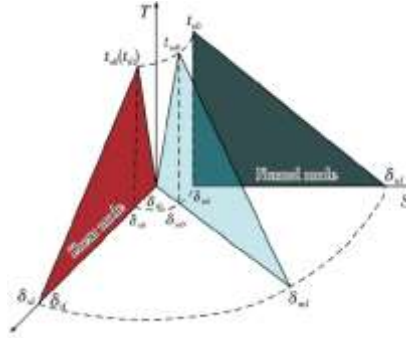
109

110

To explore the combined cracking, the quadratic normal stress criterion is applied (Equation (1)); the CZM under bilinear combined cracking is shown in Fig. 5<sup>[32]</sup> where, “ $\langle \rangle$ ”, are Macaulay brackets, means that the function has a value of zero when the independent variable is negative; the function equals the independent variable when the independent variable is positive. Macaulay brackets indicates that the initial damage does not occur in a purely compressive state of stress. The vector  $\tau$  of

111 the normal traction stress consists of three components, in which  $\tau_n$  denotes the component  
 112 perpendicular to a possibly cracked surface and  $\tau_s$  and  $\tau_t$  denote two shear components on the  
 113 surface where cracks are likely to occur.  $\tau_n^0$ ,  $\tau_s^0$ , and  $\tau_t^0$  represent the peak normal stresses. The  
 114 onset of damage occurs at  $f = 1$ .

$$115 \quad f = \left\{ \frac{\langle \tau_n \rangle}{\tau_n^0} \right\}^2 + \left\{ \frac{\tau_s}{\tau_s^0} \right\}^2 + \left\{ \frac{\tau_t^2}{\tau_t^0} \right\}^2 \quad (1)$$



116  
 117 Fig. 5 Mixed-mode cohesive traction response

118 The level of damage in a material is characterised by introducing damage variable  $D$ , which can  
 119 be defined in terms of displacement and energy. The fracture energy, that is, the energy  $G_f$  per unit  
 120 area to be absorbed in crack initiation, is used to define the damage variable. Equation (2) shows the  
 121 bilinear damage variable defined in terms of energy:

$$122 \quad D = \frac{2G_f / T_0 (\delta_{\max} - \delta_0)}{\delta_{\max} (2G_f / T_0 - \delta_0)} \quad (2)$$

123 where,  $\delta_{\max}$ ,  $\delta_0$ , and  $T_0$  denote the maximum displacement during loading, the displacement  
 124 corresponding to the onset of damage, and the critical stress under that initial damage, respectively.  
 125 The Drucker-Prager model is used for solid elements of rocks and the calculation parameters are listed  
 126 in Table 1. The rate-dependence of rock is considered in solid elements and the relationship between  
 127 the strength and strain rate is given by<sup>[33]</sup>:

$$128 \quad \sigma_d = 0.4 \sigma_{cd} (\dot{\epsilon})^{1/3} \quad (3)$$

129 where,  $\sigma_d$ ,  $\sigma_{cd}$ , and  $\dot{\epsilon}$  refer to the dynamic strength, static strength, and strain rate, respectively.

130 Table 1 CZM model parameter

Material	Density /kg·m <sup>-3</sup>	Young's modulus /GPa	Poisson' s ratio	Internal friction angle	Tensile strength /MPa	Shear strength /MPa	Fracture energy
Experimental material	1800	2.03	0.16	35	/	/	/
Cohesive	/	/	/	/	0.16	0.64	2
Anchor bolt	3000	76	0.34	/	/	/	/

131

### 132 2.3 Simulation of crack propagation

133 The solid element mesh is partitioned; thereafter, zero-thickness cohesive elements are inserted  
134 between blocks of all solid elements comprising the mesh, as shown in Fig. 6. During calculation, the  
135 elements are deleted when the damage of cohesive elements reaches 1, which means that materials  
136 are fractured to form cracks. After the crack surfaces are formed, the interaction between crack  
137 surfaces also plays an important role in the subsequent crack propagation. To prevent the interactive  
138 invasion of crack surfaces, a hard contact was automatically used on crack surfaces after cohesive  
139 elements are deleted. The Mohr-Coulomb friction model was applied as the friction criterion, with  
140 coefficient of friction  $\mu = \tan \varphi$ .

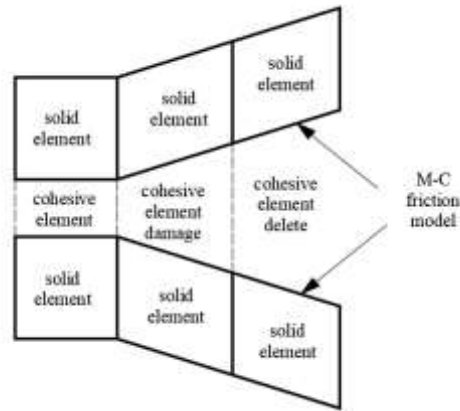


Fig. 6 Crack propagation mode

141

142

#### 143 2.4 Verification of model accuracy

144 To test the rationality of the established model and the reliability of results, the accuracy of the  
 145 model was validated by comparing the time history curves of radial stress on elements at the blast  
 146 source and the distribution of cracking at failure in the rock surrounding a cavern according to the  
 147 related test results.

148 (1) A comparison was made by selecting time history curves of pressure at two points P1 and P2  
 149 at the same positions in the model test, as shown in Fig. 7; the simulation curves obtained through  
 150 CZM undergo a shorter duration of action relative to that experimentally, mainly because materials  
 151 are idealised during numerical analysis; however, a certain discrepancy arises in cement mortars used  
 152 experimentally, which increases the duration of action of stress waves and reduces their peak intensity.  
 153 Overall, the peak stress in the simulation result approximates to that measured experimentally, and the  
 154 simulated curves are of a similar shape to their experimental counterparts, suggesting that the  
 155 simulated result is accurate.

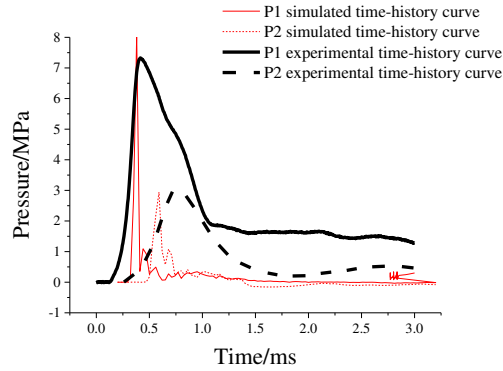
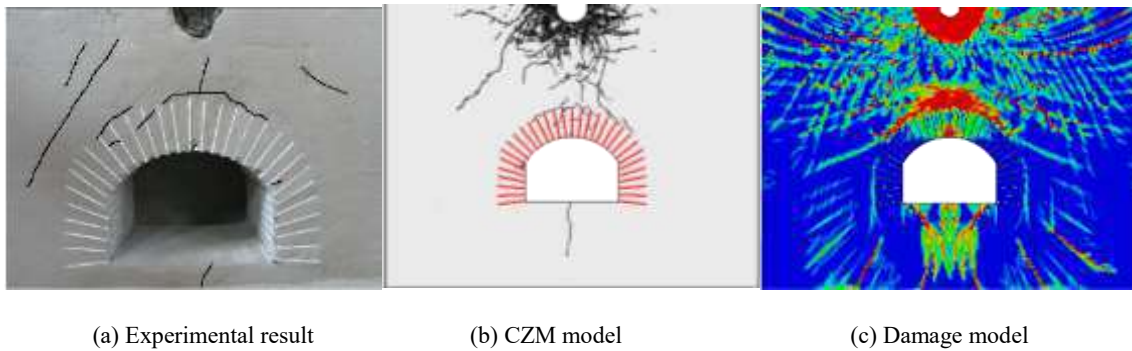


Fig. 7 Comparison of simulated and measured compressive stress time-history curves

(2) The accuracy of crack propagation simulated through the model was verified by comparing the distribution of cracks. Additionally, the physical test was assessed using the continuum damage model and the calculated result is shown in Fig. 8(c), in which the red zone corresponds to the damage zone, approximating to areas suffering formation of cracks. Figs 8(a) and (b) separately show the result obtained through the physical test and that calculated using the CZM. As shown in the figures, black parts represent the main cracks formed after blasting. By comparing the distributions of cracking across the three results, it can be found that both the damage model and CZM reflect that the most damaged zones around the anchored cavern are mainly found at the boundary and middle part of the anchored zone of the vault as well as the floor. The damage model can reveal those zones where fractures probably appear while it fails to describe the position and path of propagation of such fractures. The CZM can show the distribution and propagation of cracks, which are consistent with distributions obtained through physical testing. A broken zone is formed near the blast source, at the outer surface of which, radial cracks appear. Radial cracks generated due to blasting are deflected to the free faces and the cavern due to the presence of free faces of the top of the cavern. Vertical cracks extending to the blast source are generated at the top of the anchored zone of the cavern and cracks are formed at the boundary of the anchored zone; in addition, some fine cracks appear in the anchored zone and vertical cracks are found at the top of the cavern, arch springings, and the floor.

Above all, the reliability of the calculation model and its superiority relative to the damage model

176 are validated by comparing the time history curves of compressive stress and the distribution of cracks  
177 obtained through numerical analysis and model testing.



180 Fig. 8 Comparison of simulated damage, simulated crack and test crack

### 181 3 Analysis of crack propagation

#### 182 3.1 Crack propagation process in an anchored cavern with no pre-fabricated fractures

183 The propagation of cracks in the rock surrounding an anchored cavern without pre-fabricated  
184 fractures was analysed: Fig. 9 shows the crack propagation pattern under top explosion. Broken zones  
185 are formed around the blast source under the huge compressive stress generated by shock waves. The  
186 energy generated due to blasting is largely consumed in this stage. On this condition, the peak stress  
187 drops to below the compressive strength of the rock while it remains above the tensile strength of the  
188 rock, thus generating radial tensile cracks. The stress waves are reflected as tensile waves when  
189 propagating to the free face in the top, thus inducing spalling. As stress waves propagate to the  
190 anchored zone, fine vertical cracks occur at the ends of the bolts at the vault. In the case that stress  
191 waves are reflected as tensile waves on the free face of the vault after passing through the anchored  
192 zone, only uncoalesced fine cracks are formed in the anchored zone due to the reinforcement effect of  
193 bolts. After the reflected tensile waves propagate beyond the anchored zone, the tensile strength of  
194 rock decreases without the confining effect of the bolts beyond the anchored zone, therefore, the  
195 coalesced tensile cracks occur at the boundary between the anchored zone and the unanchored zone.  
196 The reflected tensile waves at the free faces on the top of the model and in the cavern are mutually

197 superimposed on the stress field at the tip of the radial fractures and therefore the radial fractures  
198 separately extend to the free faces forming the top and the cavern. As stress waves pass through the  
199 cavern, vertical tensile cracks are generated at the arch springings and the middle part of the floor.

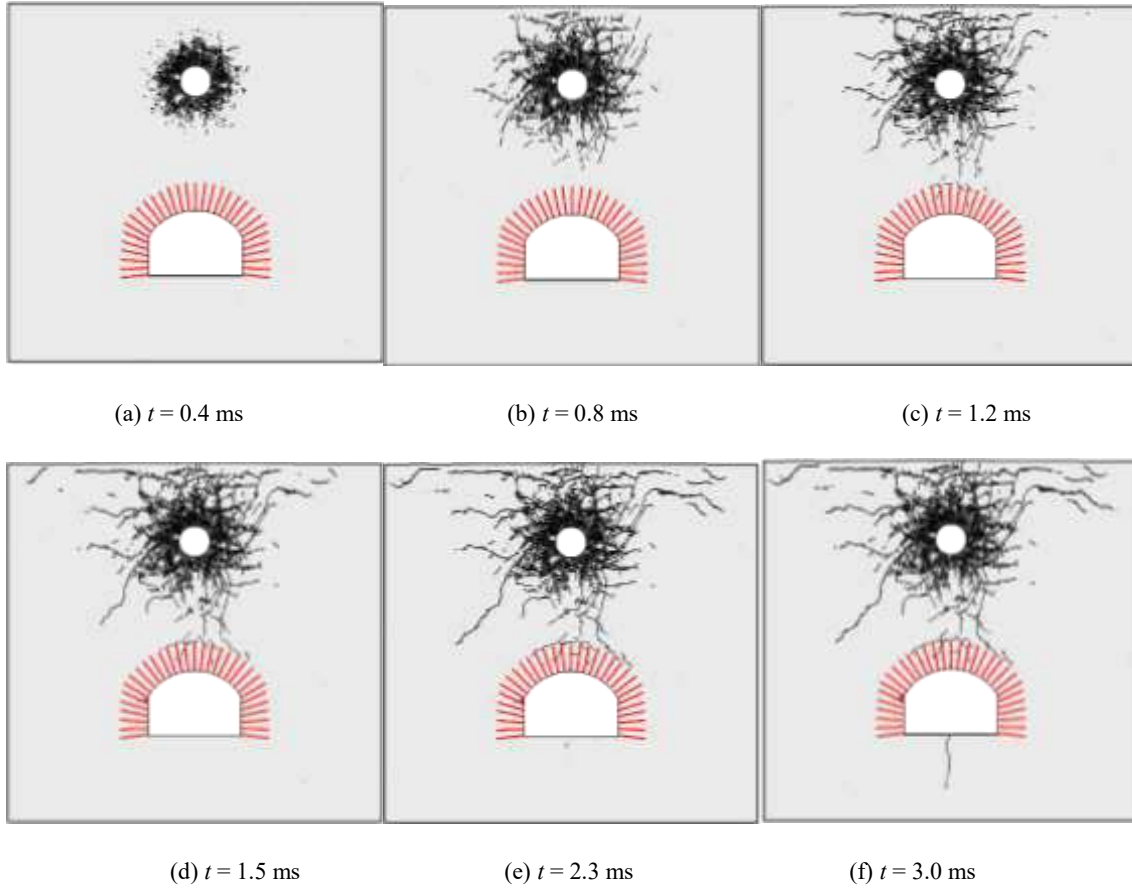


Fig. 9 Crack propagation process of anchorage cavity

### 205 3.2 Crack propagation in an anchored cavern with pre-fabricated fractures

206 Only a single fracture was established to analyse its influence on the distribution of cracks in the  
207 rock surrounding this anchored cavern. The pre-fabricated fracture, appearing as a long, narrow ellipse,  
208 was classified as an open fracture, with a short-axis length of 0.5 mm. This corresponds to an open  
209 fracture with a spacing of 5 mm in the actual cavern, showing the length of 30 cm and a skin friction  
210 coefficient of the fracture of  $\mu = \tan \varphi$ . The fracture is set beyond the anchored zone, being 39 cm  
211 from the surface of vault, with the dip angles  $\alpha$  of  $0^\circ$ ,  $30^\circ$ ,  $45^\circ$ ,  $60^\circ$ , and  $90^\circ$ , as shown in Fig. 10.

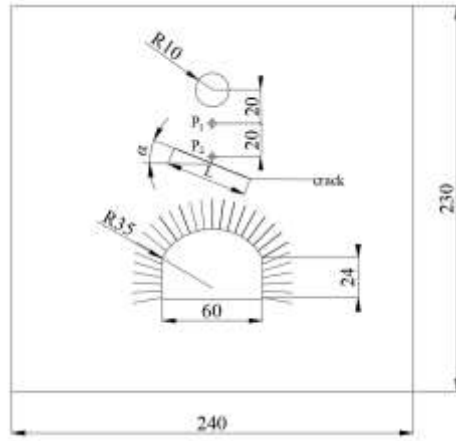


Fig. 10 Fracture setting diagram (unit: cm)

212

213

214

215

216

217

218

219

220

221

222

223

224

225

226

227

228

229

Under blast load, two forces are found at the tip of the fracture: the shear stress formed by stress waves after passing through the tip of the fracture and the tensile stress formed at the tip of the fracture. The tip of the fracture constantly advances under the effect of the two forces. The fracture can be classified as exhibiting three modes: open cracks (mode I), sliding mode crack (mode II), and tearing mode cracks (mode III). The last two fracture modes are driven by shear force, so they are also indicative of shear failure. When exploring the mechanism of formation of cracks, many scholars infer the fracture mode of materials according to the stress state in various elements. The calculation model which analyses the causes of cracks based on the proportions of different fracture energies during the failure of cohesive elements can more provide better assessments of the mode of propagation of cracks, to provide better guidance for reinforcing the rock.  $R_a$  is defined as the proportion of the shear fracture energy in the total fracture energy when cohesive elements start to be fractured:

$$R_a = 1 - \frac{G_n}{G_T} \quad (4)$$

where,  $G_n$  denotes the tensile fracture energy;  $G_T = G_s + G_t$ , in which  $G_s$  and  $G_t$  separately refer to the shear fracture energy along two conjugate directions perpendicular to the tensile stress.

The mode of propagation of cracks in surrounding rocks of the anchored cavern with a pre-fabricated fracture with a dip angle of  $45^\circ$  was analysed. Fig. 11 shows the crack formation and

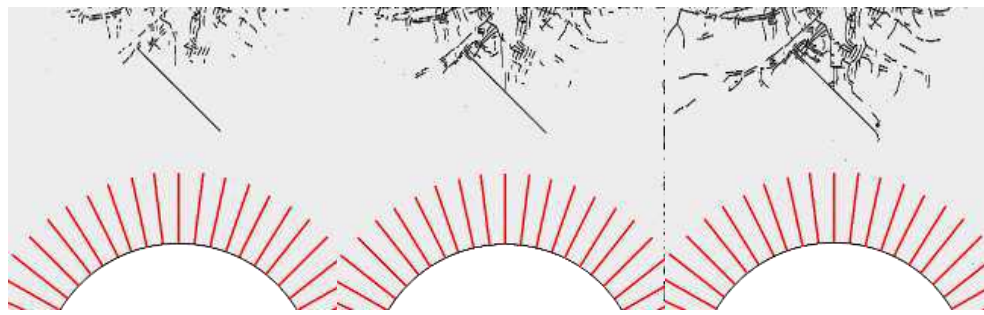
---

230 propagation process in surrounding rocks of the anchored cavern and Fig. 12 shows the fracture mode.  
231 Cracks are closed under the effect of compression, and the vertical compressive shear crack 1 is first  
232 formed from the upper part of the fracture; moreover, the tensile cracks parallel to the fracture surface  
233 are formed due to reflected tensile waves on the upper surface of the fracture, and shear cracks parallel  
234 to the direction of propagation of stress waves are formed due to closure of the fracture under  
235 compression. At the upper tip of the fracture, there are not only cracks coalescing to the fracture zone  
236 formed due to blasting but wing crack 2 extends away from the blast source, with a propagation angle  
237 of 90°. The wing crack formed at the upper tip of the fracture mainly appears as a tensile fracture;  
238 moreover, some elements with  $R_a > 0.5$  are subjected to tensile-shear fracture. This indicates that the  
239 tensile stress and shear stress synchronously influence the propagation of the crack tip and the both  
240 interact (nevertheless, tensile stress is taken as the main driving force). Crack 6 formed at the lower  
241 tip of the fracture is mainly manifest as a shear crack. When stress waves are applied to the fracture,  
242 it is dislocated, therefore, the vicinity of the lower tip of the fracture is subjected to shear failure to  
243 form short sliding-mode cracks. The tensile waves reflected from the free face of the vault are applied  
244 at the tip of the wing cracks to form a tensile fracture, which propagates towards the vault. In addition,  
245 the reflected tensile waves continue to propagate to form tensile crack 3 at the end of the wing crack  
246 at the upper tip. Cracks 4 and 5 formed under the interaction of tensile and shear failures are formed  
247 between the pre-fabricated fracture and the vault after stress waves pass through the fracture. Tensile  
248 cracks 7 and 8 are formed in the middle and right-hand side of the anchored zone of the vault.

249 According to Fig. 11, the cracks around the anchored zone in the anchored cavern with a pre-  
250 fabricated fracture mainly appear as tensile cracks under blast load, therefore, measures for preventing  
251 tensile failure are mainly taken in the vicinity of the anchored zone during its reinforcement. The  
252 cracks propagating from the middle and lower tip of the pre-fabricated fracture are shown as shear  
253 cracks and therefore reinforcement measures for their prevention should also be taken for the pre-  
254 existing fracture in the cavern.

255

256



(a)  $t = 0.4$  ms

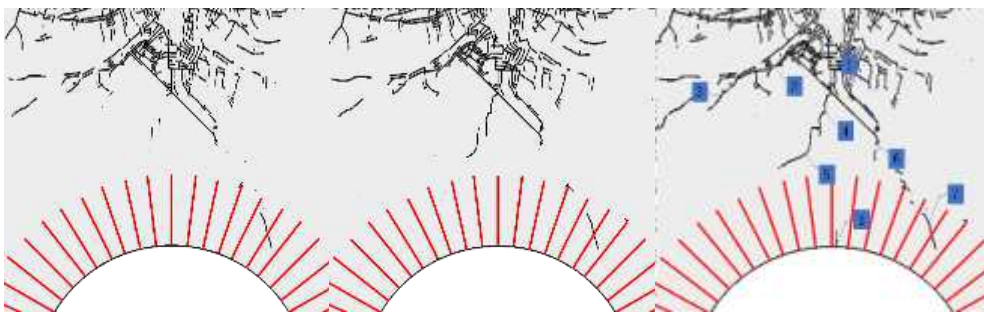
(b)  $t = 0.5$  ms

(c)  $t = 0.9$  ms

257

258

259



(d)  $t = 1.2$  ms

(e)  $t = 1.5$  ms

(f)  $t = 1.9$  ms

Fig. 11 Crack propagation process

260

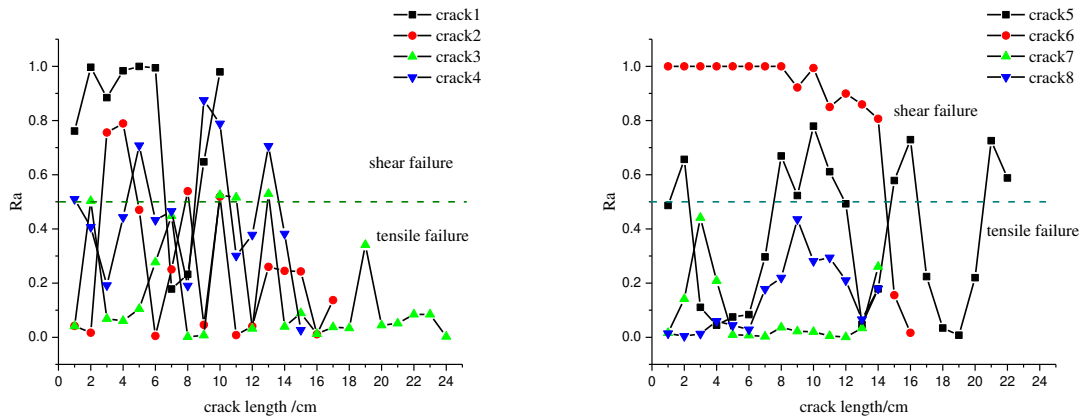


Fig. 12 Shear fracture energy ratio

261

262

263

264

265

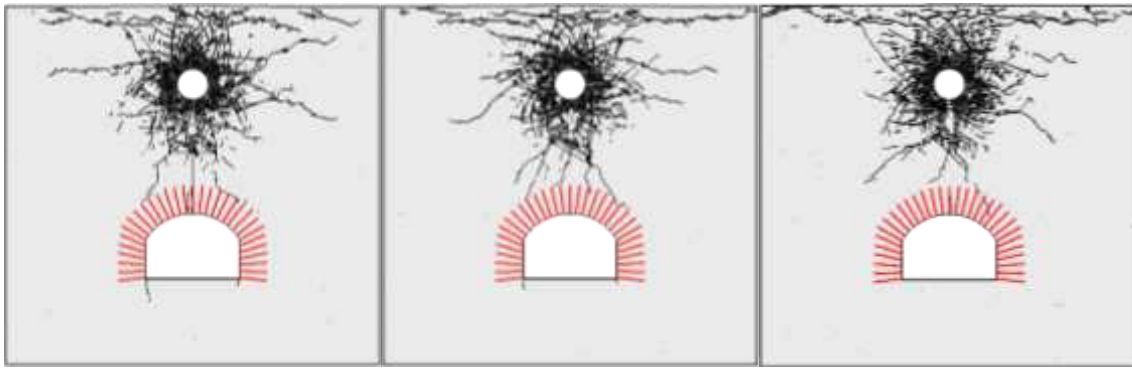
266

Figure 13 shows the distribution of cracks in surrounding rocks of the anchored cavern when a fracture with different dip angles was pre-fabricated in the top of the cavern. When the dip angle of the pre-fabricated fracture is  $0^\circ$ , the wing cracks coalesce with the tensile cracks at the boundary of the anchored zone and vertical cracks are generated along the line connecting the centre of the cracks and the centre of the vault. Moreover, the presence of the fracture changes the direction of propagation

---

267 of stress waves and attenuates the energy generated by stress waves. Therefore, no reflected tensile  
268 cracks are formed in the middle part of the boundary of the anchored zone of the vault while cracks  
269 are found only in the two sides. Within the anchored zone of the vault, vertical cracks are generated  
270 only at the top while compressive shear cracks appear in corners of the two side walls. As the dip  
271 angle of the pre-fabricated fracture increases, the cracks at the boundary of the anchored zone in the  
272 left-hand end far from the fracture are gradually reduced and deflected away from the cavern; however,  
273 the opposite trend is seen in the right-hand end of the anchored zone. At a dip angle of the pre-  
274 fabricated fracture of  $45^\circ$ , the wing cracks at the left-hand end of the fracture do not coalesce to the  
275 boundary of the anchored zone while cracks occur in the right half of the anchored zone of the vault.  
276 No cracks are formed in the arch foot and floor, which implies that the presence of the pre-fabricated  
277 fracture attenuates stress waves and the generation of numerous cracks above the fracture absorbs  
278 some of the energy generated by stress waves. When the dip angle of the fracture exceeds  $45^\circ$ , the  
279 cracks formed at the left-hand end of the fracture coalesce with those at the boundary of the anchored  
280 zone. Owing to the right-hand end of the fracture being close to the anchored zone of the cavern, wing  
281 cracks coalesce with the reflected cracks at the boundary of the anchored zone and vertical cracks are  
282 also present in the middle of the floor. When the pre-fabricated fracture is vertical, vertical cracks  
283 parallel to the fracture are formed from the upper end of the cracks. The distribution of cracks around  
284 the cavern is similar to that in the anchored cavern with no pre-fabricated fracture. This is because the  
285 fracture is parallel to the direction of propagation of the stress waves and exerts no significant  
286 influence on the propagation of stress waves.

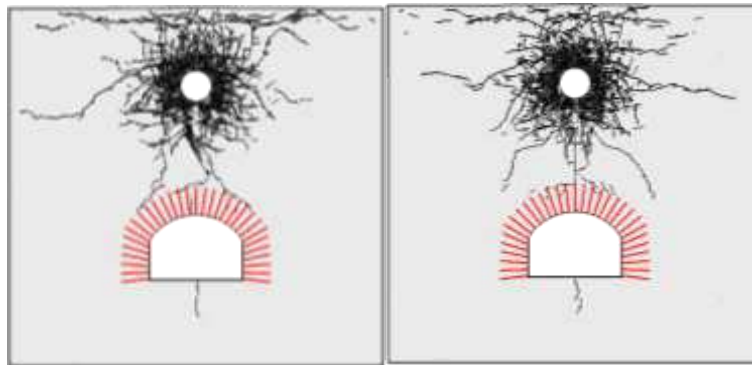
287



(a)  $\alpha = 0^\circ$

(b)  $\alpha = 30^\circ$

(c)  $\alpha = 45^\circ$



(d)  $\alpha = 60^\circ$

(e)  $\alpha = 90^\circ$

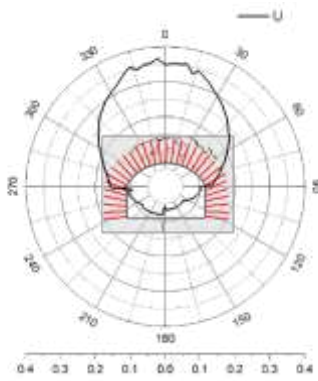
Fig. 13 The crack distribution around an anchored cavity with cracks at different dip angles

#### 4 Analysis of the dynamic response of an anchored cavern

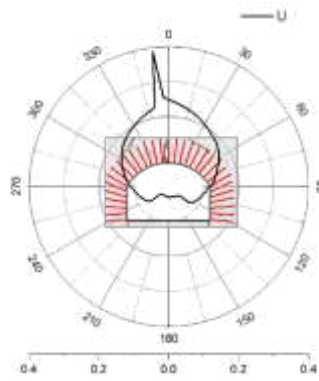
##### 4.1 Analysis of the vault displacement in an anchored cavern

Figure 14 shows the distribution of peak displacements in the rock surrounding an anchored cavern, in which  $0^\circ$  and  $180^\circ$  separately correspond to the centres of the vault and floor while  $90^\circ$  and  $270^\circ$  separately correspond to the arch springings. The peak displacement of the vault facing the blast effect is the largest, successively followed by that of the side walls and floor. When no fracture or a fracture is pre-fabricated vertically in the vault, the displacement of the floor exceeds that of the side walls while the former is lower than the latter on condition that the pre-fabricated fracture is inclined; moreover, the displacements of the arch springing and side wall in the right-hand side closer to the pre-fabricated fracture are slightly larger than those on the left. The distributions of the peak displacement are smooth and continuous and the zone of abruptly changing displacement corresponds

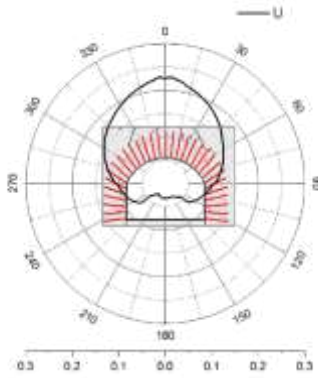
304 to the surrounding rocks within which cracks are generated. When the surrounding rocks are exfoliated,  
305 the displacement in the corresponding areas increases significantly, for example, the zone with  
306 abruptly changing displacement on the vault of the cavern having a pre-fabricated fracture with the  
307 dip angle of  $0^\circ$ . On condition that many cracks are present at the boundary and the interior of the  
308 anchored zone, the displacement of the corresponding surrounding rocks also increases slightly,  
309 indicating that the displacement of the surrounding rocks is somewhat related to the displacement of  
310 the cracks.



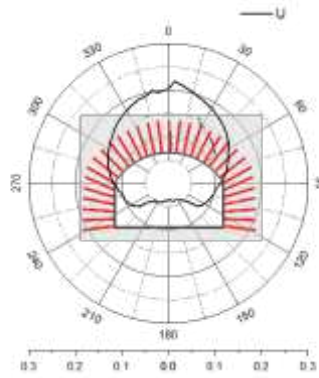
311  
312 (a) No crack



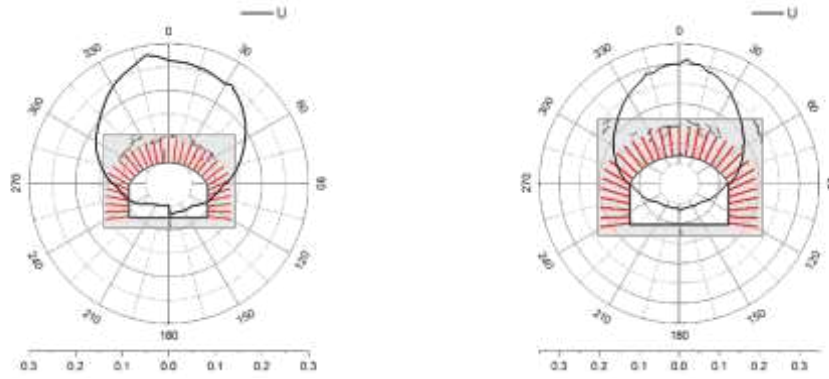
(b)  $\alpha = 0^\circ$



313  
314 (c)  $\alpha = 30^\circ$



(d)  $\alpha = 45^\circ$



(e)  $\alpha = 60^\circ$

(f)  $\alpha = 90^\circ$

Fig. 14 Cavern peak displacement distribution

315

316

317

318

319

320

321

322

323

324

325

326

327

328

329

330

331

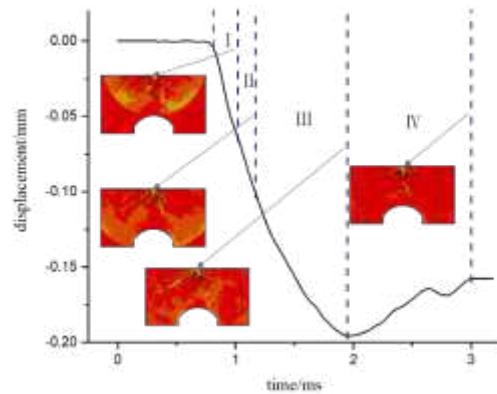
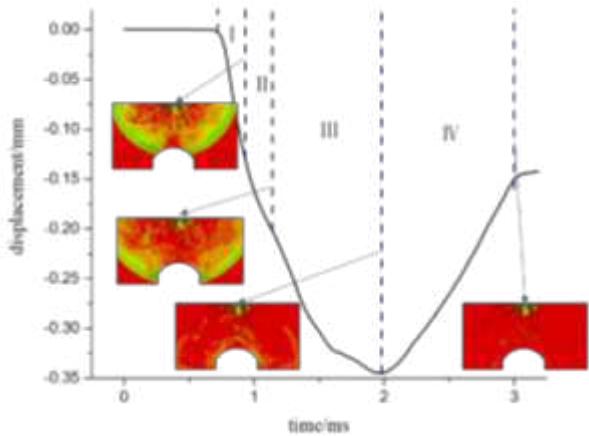
332

333

334

Figures 15 and 16 separately show the displacements of the vault of an anchored cavern without a fracture and with a pre-fabricated fracture at a dip angle of  $45^\circ$ . A negative represents a downwards displacement. The results obtained experimentally and by numerical calculation reveal that the dynamic response of the anchored cavern ends 3 ms after blasting and thus the displacement at 3 ms is selected as the residual displacement. The vault displacement is divided into four phases: in phase I, the vault is deformed under the effect of stress waves and no cracks occur in the anchored zone of the vault. The deformation is manifest as elasto-plastic deformation of the upper part of the cavern. The deformation is insignificant in this phase. In phase II, cracks are found in the anchored zone; however, there are only a small number of cracks therein and the vault displacement is low. In phase III, cracks occur outside the anchored zone. After the reflected waves from the free face of the vault pass out of the anchored zone, numerous cracks are formed at the boundary of the anchored zone. The vault displacement occurs mainly in this phase. In phase IV, the elastic displacement recovers. The elastic deformation in rocks and that of bolts for the anchored zone gradually recover and therefore the vault will be displaced upwards to some extent. As shown in Figs 14 and 15, the vault displacement of the anchored cavern with a pre-fabricated fracture starts to change later because the presence of the fracture hinders the propagation of stress waves. Therefore, the vault displacement begins to vary later; moreover, the presence of the fracture attenuates stress waves and thus the displacement of the

335 anchored cavern with a pre-fabricated fracture is lower than that without a fracture in phase I. As for  
 336 the anchored cavern with a pre-fabricated fracture, the cracks around the fracture continue to  
 337 propagate under the effect of reflected waves in phase III; in addition, the recovered displacement is  
 338 lower than that of the anchored cavern without the fracture in phase IV. The reason for this is that the  
 339 presence of many cracks around the pre-fabricated fracture in the vault weakens the rock in the upper  
 340 part, leading to a large residual displacement. It can be seen from Table 2 that the peak displacements  
 341 all decrease slightly when a fracture is pre-fabricated in the vault compared with those of the anchored  
 342 cavern without a fracture, in which the peak displacement is the lowest when the dip angle of the pre-  
 343 fabricated fracture is 45°; the residual displacements of the anchored cavern with a pre-fabricated  
 344 fracture are all larger than those without a fracture, except when the dip angle of the fracture is 0°, in  
 345 which the residual displacement reaches its maximum at a dip angle of 90°.



346 Fig. 15 Displacement of the vault of an unfractured cavern

347 Fig. 16 Displacement of the vault of a cavern with a

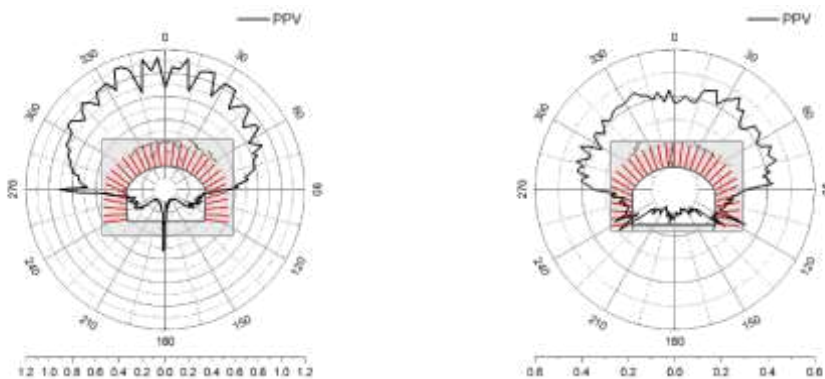
348 crack

349 Table 2 Vault displacement

Dip angle	No crack	0°	30°	45°	60°	90°
Peak displacement	0.347	0.233	0.207	0.195	0.260	0.295
Residual displacement	0.149	0.137	0.156	0.157	0.151	0.235

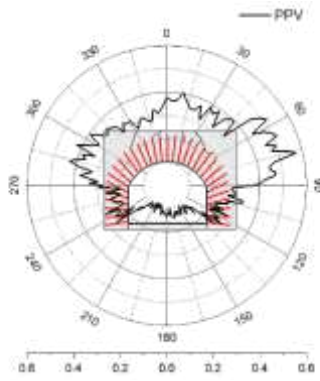
350 4.2 Analysis of the particle velocity in an anchored cavern

351 Figure 17 shows the distribution of PPVs around an anchored cavern, in which  $0^\circ$  and  $180^\circ$   
352 separately correspond to the centres of the vault and floor while  $90^\circ$  and  $270^\circ$  separately correspond  
353 to arch springings. The distribution of the PPV appears serrated, positions with a low PPV correspond  
354 to those reinforced by bolts while the zones of lower reinforcement effect between adjacent bolts have  
355 a larger PPV, indicating that bolts reduce the PPV around parts of the cavern. For an anchored cavern  
356 without a pre-fabricated fracture, the PPVs are quasi-symmetrically distributed, in which the PPV is  
357 largest in the vault, successively followed by that in the side walls and floor: however, due to the  
358 differences in the distribution of cracks in surrounding rocks, the PPV abruptly changes in local zones  
359 where cracks appear. For example, spalling or radial cracks are formed in the left-hand arch springing  
360 and the centre of the floor, where the PPV increases the most. The PPV decreases significantly when  
361 a pre-fabricated fracture is present in the upper part of the vault. With increasing dip angle of the pre-  
362 fabricated fracture, the PPV distribution in the surrounding rocks becomes asymmetric: the PPV in  
363 the anchored zone in the right-hand end closer to the pre-fabricated fracture is larger owing to more  
364 cracks being generated in this zone. Above all, the PPV in surrounding rocks is the lowest when a  
365 horizontal fracture is pre-fabricated in the vault; the PPV in surrounding rocks for a dip angle of the  
366 pre-fabricated fracture of  $90^\circ$  approximates to that of the anchored cavern without such a fracture;  
367 however, the PPV is also slightly lower than that of the anchored cavern without the fracture due to  
368 energy absorption along the pre-fabricated fracture.

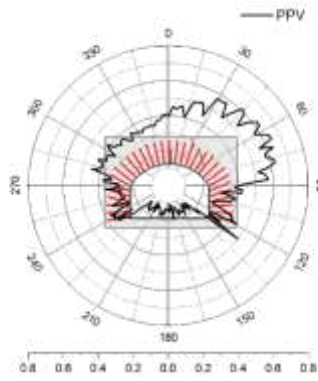


370

(a) No crack



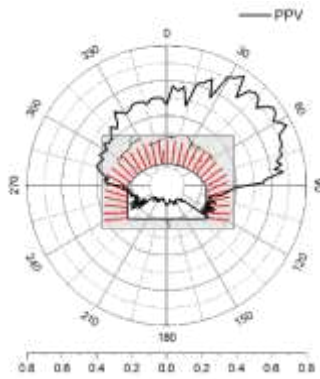
(b)  $\alpha = 0^\circ$



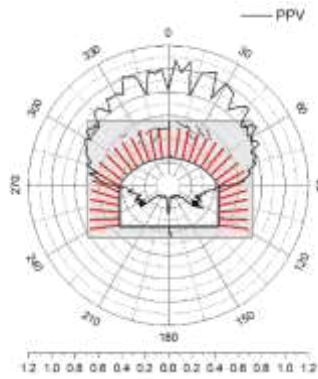
371

372

(c)  $\alpha = 30^\circ$



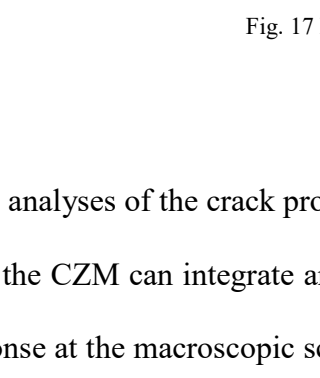
(d)  $\alpha = 45^\circ$



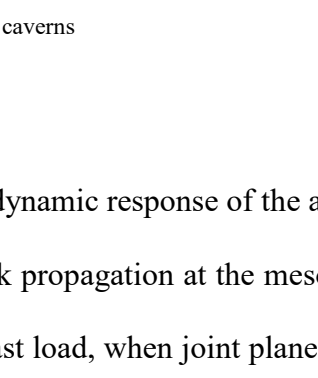
373

374

(e)  $\alpha = 60^\circ$



(f)  $\alpha = 90^\circ$



375

Fig. 17 PPV distribution in caverns

## 376 5 Discussion

377 According to analyses of the crack propagation and dynamic response of the anchored cavern, it  
378 can be found that the CZM can integrate analysis of crack propagation at the mesoscopic scale with  
379 the dynamic response at the macroscopic scale. Under blast load, when joint planes such as fractures  
380 are present on the top of the cavern, they give rise to two effects on the stability of the cavern: on the  
381 one hand, the fractures block the propagation of stress waves, especially open fractures. Numerous  
382 propagating fractures are present in the vicinity of pre-existing fractures, absorbing much of the energy  
383 associated with the input stress waves; on the other hand, fractures weaken the rock in the upper part,  
384 resulting in increasing residual displacement of the vault.

---

385 According to the distribution of PPV in surrounding rocks of the cavern, it can be found that bolts  
386 decrease the PPV and act to restrain crack propagation. The existing safety criterion applied during  
387 blasting vibration is mainly discussed in relation to unsupported caverns. According to Fig. 15, cracks  
388 have been formed in the floor of the cavern that is unreinforced by bolts at a low PPV; by contrast, a  
389 larger PPV is required to form cracks in the anchored zone. The model shows a similarity ratio of 0.3.  
390 By transforming the vibration velocity into that during practical engineering operations, cracks occur  
391 in the unanchored zone at a PPV of 60 cm/s, which is similar to those found elsewhere [34,35,36,37]  
392 However, the PPV must reach about 120 cm/s (about three times that in the unanchored zone) so that  
393 cracks can be generated in the reinforced (anchored) zone, therefore, it is necessary to explore the safe  
394 vibration velocity during blasting in an anchored cavern.

395

## 396 **6 Conclusion**

397 Based on a CZM, the crack distribution and propagation in an anchored cavern without and with  
398 a pre-fabricated fracture at different dip angles under blast load were simulated by globally embedding  
399 cohesive elements with zero thickness. In this way, the feasibility of using the CZM to simulate the  
400 fracture and failure of caverns was validated; moreover, a comparison was undertaken between the  
401 influences of the dip angles of the pre-fabricated fracture in the vault on the crack propagation and  
402 dynamic response. The following conclusions are drawn:

403 (1) The CZM can simulate the cracking and propagation of cracks by embedding cohesive  
404 elements with zero thickness between solid elements. By comparing with the physical test, the CZM  
405 simulates the distribution of cracks in an anchored cavern without a pre-fabricated fracture.  
406 Additionally, the feasibility of the model when used to simulate crack propagation in an anchored  
407 cavern is verified.

408 (2) Under top explosion, cracks around the anchored cavern without a pre-fabricated fracture

---

409 mainly occur at the boundary of the anchored zone of the vault, arch springing, and the middle of the  
410 floor. When a pre-fabricated fracture is present in the vault, numerous reflected tensile cracks and  
411 vertical shear cracks are formed above the fracture due to the blocking effect of the fracture on stress  
412 waves. In addition, wing cracks are formed at the tip of the fracture; the number and extent of reflected  
413 tensile cracks at the boundary of the anchored zone of the vault decrease significantly, decreasing at  
414 first, then increasing with increasing dip angle of the pre-fabricated fracture. There are fewest cracks  
415 at the boundary of the anchored zone at a dip angle of  $45^\circ$ . Tensile cracks are mainly found around the  
416 anchored zone while shear cracks also appear in the vicinity of the pre-fabricated fracture. When  
417 reinforcing surrounding rocks, measures should be taken in the vicinity of the anchored zone to  
418 prevent tensile failure; by contrast, the reinforcement measures used for preventing shear failure  
419 should be also taken as for pre-existing fractures in the cavern.

420 (3) Under blast load, the vault displacement of the anchored cavern is mainly attributed to tensile  
421 cracks formed in the anchored zone due to the reflected tensile waves on the free face of the vault.  
422 When a fracture is pre-fabricated in the upper part of the vault, the blocking effect of the fracture on  
423 stress waves leads to the reduction of the peak displacement of the vault; moreover, the presence of  
424 the fracture weakens the rock in the upper part, resulting in greater residual displacement.

425 (4) The distribution of PPV in the anchored cavern is serrated: the vibration velocity in the  
426 anchored zone is lower than that in the unanchored zone. In terms of the overall distribution of PVV,  
427 the vault shows the largest PVV, successively followed by the side walls and the floor. In addition, the  
428 PVV increases abruptly in positions subjected to spalling and cracking. When a pre-fabricated fracture  
429 is present in the upper part of the vault, the PVV decreases significantly; the PVV in the right half of  
430 the anchored zone closer to the pre-fabricated fracture is larger than that on the left. The lowest PVV  
431 in surrounding rocks occurs when a pre-fabricated fracture is established in the horizontal direction.  
432 The PVV enabling formation of cracks in the anchored zone is about three times larger than that in  
433 the unanchored zone.

---

434 **Acknowledgment**

435 This work was supported by the National Natural Science Foundation of China (Grant No.  
436 51779197), the Natural Science Foundation of Hainan Province (Grant No. 420QN291), and the  
437 Sanya Yazhou Bay Science and Technology City Administration Scientific research project (No.  
438 SKJC-KJ-2019KY02).The authors would like to thank the editors and reviewer for their careful  
439 review of this paper.

440 **References**

- 441 [1] Fei Xue, Caichu Xia, Guoliang Li, Baocheng Jin, Yongwang He, Yapeng Fu, Tayfun Dede.  
442 Safety Threshold Determination for Blasting Vibration of the Lining in Existing Tunnels under  
443 Adjacent Tunnel Blasting[J]. Advances in Civil Engineering,2019.
- 444 [2] Zhang Z, Zhou C, Remennikov A, et al. Dynamic response and safety control of civil air  
445 defense tunnel under excavation blasting of subway tunnel[J]. Tunnelling and Underground  
446 Space Technology incorporating Trenchless Technology Research, 2021,112.
- 447 [3] V. Molkov,W. Dery. The blast wave decay correlation for hydrogen tank rupture in a tunnel fire[J].  
448 International Journal of Hydrogen Energy,2020.
- 449 [4] LIU Shaoliu, SUN Huixiang, WANG Xiaolong. Research on the Numerical Simulation of  
450 Penetration Effect of Underground Cavity with Different Spans [J]. Journal of Projectiles,  
451 Rockets, Missiles and Guidance, 2017, 37(04): 51-54+59.
- 452 [5] Jingmao X , Jincai G , Anmin C , et al. Model Test on Failure Modes of Anchorage Tunnels  
453 Subjected to Blast Loading[J]. Journal of Engineering Science & Technology Review, 2018,  
454 11(4):118-125.
- 455 [6] WANG Guangyong, GU Jincai, CHEN Anmin,et al. Failure modes and process of tunnels  
456 reinforced by rockbolts under top explosion [J]. Chinese Journal of Geotechnical

- 
- 457        Engineering,2015,37(8): 1381-1389.
- 458 [7] Sivalingam Koneshwaran, David P. Thambiratnam, Chaminda Gallage. Blast Response of  
459        Segmented Bored Tunnel using Coupled SPH–FE Method. 2015, 2:58-71.
- 460 [8] X. Xia, H.B. Li, J.C. Li,B. Liu, C. Yu. A case study on rock damage prediction and control  
461        method for underground tunnels subjected to adjacent excavation blasting[J]. Tunnelling and  
462        Underground Space Technology incorporating Trenchless Technology Research,2013,35.
- 463 [9] Xudong Li, Kewei Liu, Jiakai Yang, Roberto Nascimbene. Study of the Rock Crack Propagation  
464        Induced by Blasting with a Decoupled Charge under High In Situ Stress[J]. Advances in Civil  
465        Engineering,2020.
- 466 [10]    Bang Liu, Zheming Zhu, Ruifeng Liu,Lei Zhou, Duanying Wan, Radoslaw Zimroz. Study  
467        on the Fracture Behavior of Cracks Emanating from Tunnel Spandrel under Blasting Loads by  
468        Using TMCSC Specimens[J]. Shock and Vibration,2019,2019.
- 469 [11]    Zhou Wei, Tang Longwen, Liu Xinhong ,et al., Mesoscopic simulation of the dynamic  
470        tensile behavior of concrete based on a rate-dependent cohesive model. International Journal of  
471        Impact Engineering, 2016. 95: p. 165-175.
- 472 [12]    GUO Dongming, Liu Kang, YANG Renshu ,et al. Simulation experiments on the  
473        mechanism of adjacent tunnel crack extension induced by explosion load [J].Journal of  
474        Vibration and shock,2016,35(2):178-183.
- 475 [13]    Yang R , Wang Y , Guo D , et al. Experimental Research of Crack Propagation in Polymethyl  
476        Methacrylate Material Containing Flaws Under Explosive Stress Waves[J]. Journal of Testing &  
477        Evaluation, 2016, 44(1):248-257.
- 478 [14]    Jianchun Li, Guowei Ma. Analysis of Blast Wave Interaction with a Rock Joint[J]. Rock

- 
- 479 Mechanics and Rock Engineering,2010,43(6).
- 480 [15] Deng X F , Zhu J B , Chen S G , et al. Numerical study on tunnel damage subject to blast-  
481 induced shock wave in jointed rock masses[J]. Tunnelling and Underground Space Technology,  
482 2014, 43(6):88-100.
- 483 [16] Choi Byung Hee, Kang Myoung Soo, Ryu Chang Ha, Kim Jae Woong. Explosion  
484 Modelling for Crack Propagation near Blast holes in Rock Plate[J]. Explosives and  
485 Blasting,2015,33(1).
- 486 [17] Chenglong He,Jun Yang. Experimental and numerical investigations of dynamic failure  
487 process in rock under blast loading[J]. Tunnelling and Underground Space Technology  
488 incorporating Trenchless Technology Research,2018.
- 489 [18] Yixian Wang, Siyao Wang, Yanlin Zhao, Panpan Guo, Yan Liu, Ping Cao, Xinglin Lei. Blast  
490 Induced Crack Propagation and Damage Accumulation in Rock Mass Containing Initial  
491 Damage[J]. Shock and Vibration,2018.
- 492 [19] JunHong Huang, XinPing Li, Yi Luo, TingTing Liu, Qian Dong, Kun Xu, ChuXuan Tang.  
493 Numerical simulation of influence of filled joint on the crack formed by notch hole blast[J].  
494 European Journal of Environmental and Civil Engineering,2020,24(4).
- 495 [20] Xudong Li, Kewei Liu, Jiakai Yang, Roberto Nascimbene. Study of the Rock Crack  
496 Propagation Induced by Blasting with a Decoupled Charge under High In Situ Stress[J].  
497 Advances in Civil Engineering,2020.
- 498 [21] M. B, G. S, B. K H. Numerical direct shear tests to model the shear behaviour of rock joints[J].  
499 Computers and Geotechnics, 2013,51.
- 500 [22] R. Pramanik,D. Deb. Implementation of Smoothed Particle Hydrodynamics for Detonation

- 
- 501 of Explosive with Application to Rock Fragmentation[J]. Rock Mechanics and Rock  
502 Engineering,2015,48(4).
- 503 [23] Navid B, Peter K K. Numerical investigation of the influence of specimen size on the  
504 unconfined strength of defected rocks[J]. Computers and Geotechnics, 2016,77.
- 505 [24] Barenblatt G I. The mathematical theory of equilibrium cracks in brittle fracture[J].  
506 Advances in applied mechanics, 1962, 7: 55-129.
- 507 [25] Dugdale D S. Yielding of steel sheets containing slits[J]. Journal of the Mechanics and  
508 Physics of Solids, 1960, 8(2): 100-104.
- 509 [26] Ma, G., W. Zhou and X. Chang, Modeling the particle breakage of rockfill materials with  
510 the cohesive crack model. Computers and Geotechnics, 2014. 61: p. 132-143.
- 511 [27] Zhou Wei, Tang Longwen, Liu Xinhong ,et al., Mesoscopic simulation of the dynamic  
512 tensile behavior of concrete based on a rate-dependent cohesive model. International Journal of  
513 Impact Engineering, 2016. 95: p. 165-175. 18.
- 514 [28] Wang X F, Yang Z J, Yates J R, et al. Monte Carlo simulations of mesoscale fracture  
515 modelling of concrete with random aggregates and pores[J]. Construction and Building  
516 Materials, 2015, 75: 35-45.
- 517 [29] Snozzi L, Caballero A, Molinari J F. Influence of the meso-structure in dynamic fracture  
518 simulation of concrete under tensile loading[J]. Cement and Concrete Research, 2011, 41(11):  
519 1130-1142.
- 520 [30] Hongxiang Jiang and Deguang Meng. 3D numerical modelling of rock fracture with a  
521 hybrid finite and cohesive element method[J]. Engineering Fracture Mechanics, 2018, 199 :  
522 280-293.

- 
- 523 [31] Hidehiko Toyama and Hiroshi Kishida and Akio Yonezu. Characterization of fatigue crack  
524 growth of concrete mortar under cyclic indentation loading[J]. Engineering Failure Analysis,  
525 2018, 83 : 156-166.
- 526 [32] ZHOU Rui, LIU Zhongwang, ZHANG Jianguo. Three-dimensional Numerical Simulation  
527 of Green Metal Powder Compacts Crack Based on DPC-CZM Mixed Model [J]. Materials  
528 Reports,2020,34(06):6151-6155.
- 529 [33] R.H. Price, P.J. Boyd, J.S. Noel, R.J. Martin, Relation between static and dynamic rock  
530 properties in welded and nonwelded tuff, in: P.P. Nelson, S.E. Laubach (Eds.), Rock Mechanics,  
531 AA Balkema, Rotterdam, 1994.
- 532 [34] BAUER A, CALDER P N.Open Pit and Blast Seminar[R].Course No.63221, Kingston,  
533 Ontario, Canada:Min-ing Engineering Department, Queens University, 1978.
- 534 [35] HOLMBERG R, PERSSON P A.The Swedish Approach to Contour Blasting[C] //  
535 Proceedings of the 4th Confer-ence on Explosive and Blasting Technique.[S.l.]:[s.n.], 1978:113-  
536 127.
- 537 [36] MOJTABAI N, BEATTIE S G.Empirical Approach to Prediction of Damage in Bench  
538 Blasting[J].Trans InstMin and Metall Sect A, 1996, 105:A75-A80.
- 539 [37] The Modern Technique of Rock Blasting. LANGEFORS U,KIHLSTROM B. John  
540 Wiley&Sons Inc . 1973

541